Reverse drag: Host rock deformation during slip along existing faults

Oded Katz[a] and Ze'ev Reches[b]
[a]Geological Survey of Israel, 30 Malkhe Yisrael Street, Jerusalem 95501, Israel
[b]School of Geology and Geophysics, University of Oklahoma, Norman, OK 73019, USA

(Received 15 March 2005 and in revised form 22 June 2006)

ABSTRACT

Katz, O. and Reches, Z. 2006. Reverse drag: Host rock deformation during slip along existing faults. Isr. J. Earth Sci. 55: 43–53.

Faults are typically weaker than the surrounding host rocks, hence it is anticipated that loading a faulted rock body will cause slip along existing faults while the fault-bounded blocks should remain undeformed. We present here field, experimental, and numerical observations that profoundly deviate from the above concept. The field observations are from the Negev (southern Israel), on the western side of the Dead Sea rift, and are related to the intra-plate deformation. We found that (1) the host rock along existing faults may undergo significant deformation during slip along these faults; (2) the syn-slip strain may have the opposite sense of shear with respect to the sense of shear along the fault (commonly known as "reverse drag"); (3) the strain of the host rock adjacent to the faults increases with increasing fault slip; (4) this strain is restricted to a region extending 5–10% of the fault length on each side of the fault, and it decreases non-linearly with distance from the fault; and (5) the above deformation features were observed in host rock of elastic, viscous, or plastic rheology.

1. INTRODUCTION

Fault-zones and their surroundings are enriched in many secondary structures that are related to faulting, for example, microcracks, gouge zones, joints, secondary faults, shear zones, and flexures (e.g., Aydin and Johnson, 1978; Suppe, 1985; Chester and Logan, 1986; Lyakhovsky et al., 1997; Vermilye and Scholz, 1998; Katz et al., 2003). The present study addresses one of the more puzzling structures associated with faults: flexed planar rock bodies close to faults. These flexures are commonly known as "fault drag", (Davis and Reynolds, 1996), "reverse drag" (Hamblin, 1965; Reches and Eidelman, 1995), or "flanking structures" (Passchier, 2001).

The development of flexures close to faults was clearly displayed in the experiments of Freund (1974). The initial configuration of the experiments included plasticene cakes with a set of pre-cut faults and continuous linear markers traced at 60° to the faults (Fig. 1a). These cakes were subjected to 2D pure-shear shortening as high as –0.5 (Fig. 1b). During the deformation, the initially linear markers were displaced by slip along the faults and were flexed adjacent to the faults (e.g., points marked by R in Fig. 1b). The flexure opens gradually away from the faults until the markers approach linear shape, as portrayed schematically in Fig. 1c. Figure 1c displays three flexed layers (thick solid lines on both sides of the fault), and the original, planar layers prior to flexing (dashed thin lines on the right block). The spatial association of the flexure with the fault and the symmetry of the flexures on both sides

E-mail: odedk@gsi.gov.il

 0021-2164/06 $4.00

of the faults indicate that the flexure is genetically related to the slip along the fault.

The genetic relations, however, are puzzling. In the view of Fig. 1c, the sense of slip along the fault is *left-lateral* (black arrows) as is apparent from the sense of separation. Consider now the sense of shear that is needed to flex the layers from planar shape (thin, dashed lines) into the flexed shape (thick curves). The simple kinematic relations indicate that *right-handed* shear (gray arrows) is needed to flex the layers into their current shape. This observation implies that the rocks at the immediate proximity of the faults underwent shear sense that is *opposite* to the sense of shear associated with the slip along the fault. Following previous works (e.g., Hamblin, 1965), we refer to this phenomenon as "reverse drag".

In this study, we first present evidence for reverse drag along faults within the quartz-syenite intrusion of the Ramon area, southern Israel. We continue with the analysis of the geometry of the reverse drag, and investigate the mechanism of its formation through comparison with other field, experimental, and numerical cases. We emphasize the timing of reverse drag with respect to the faulting and its relation to the rheology of the host rocks.

2. REVERSE DRAG ALONG FAULTS IN GEVANIM DOME, SOUTHERN ISRAEL

The geometry of the studied faults

The N–S-trending fault set, mapped and analyzed within the quartz-syenite intrusion by Katz et al. (2003), consists of linked and segmented faults, 1–100 m long, with a right lateral displacement ranging from few millimeters to over a meter. The deformation features across the faults were zoned (following Caine et al., 1996) into a central fault core with a width of 0.001 of fault length, through a damage zone to the protolith with no fault-related deformation at a distance of 0.05–0.06 of fault length. The fault core consists of breccia and is highly sheared (up to 500% strain). The damage zone consists of tensile and shear microfractures and reveals competence reduction of 30–50% (studied using a Schmidt hammer). A marked absence of intragranular distributed tensile microcracks was observed in microscopic analysis of core samples close to the above faults (Katz et al., 2003) as well as in laboratory samples loaded to failure (Katz, 2002).

The current analysis focused on two faults of the N–S fault set that are marked GF2 and GF3 (after Katz

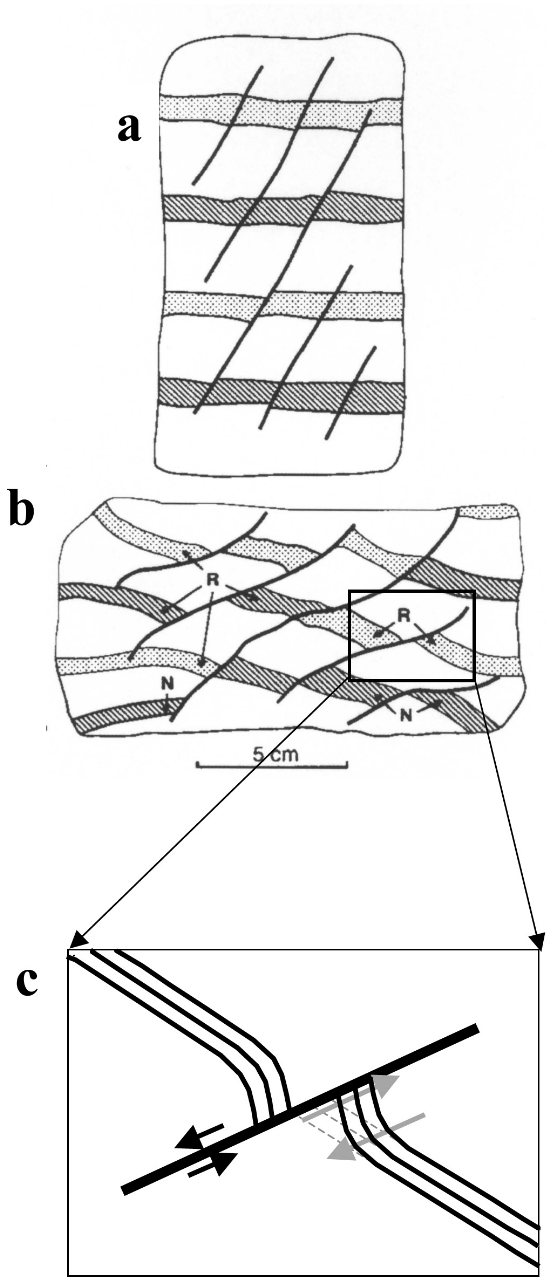

Fig. 1. Flexing of layers at fault proximity. (a, b) Passive lines displaced and distorted by small faults in deformed plasticene cake; R points to reverse drag (after Freund, 1974). (a) Before and (b) after pure shear shortening as high as –0.5. (c) A line drawing of (a). Note the reverse drag: the sense of slip along the fault is *left-lateral* (black arrows) as apparent from the sense of separation; the sense of shear that is needed to flex the layers from planar shape (thin, dashed lines) into the flexed shape (thick curves) is *right-handed* (gray arrows).

et al., 2003). The mapped trace of GF2 is about 7.5 m long with a clearly exposed northern tip and a poorly exposed southern one (Fig. 2a). GF2 displays four segments, 1.2 m to 2.6 m long with local trends from 350° to 010°. Right-lateral slip along GF2 (measured using offset fault-normal fracture—Fig. 2b) increases from zero at the northern tip to an approximately constant value of 19.0 ± 3.0 mm along its central part. The fault zone of GF2 is 1 mm to 20 mm wide, with several portions of brecciated, crushed host rock. GF3 is an order of magnitude longer than GF2, with an exposed trace of 100 m (probably longer) and general trend of NNW (Fig. 3a). GF3 consists of at least ten segments with lengths of 2 m to 38 m, local trends of NNE (015°) to NNW (340°), and measured slip magnitude of 25 cm to 125 cm (Katz et al., 2003). The fault zone width of GF3 is up to 0.5 m, and consists of two major breccia zones up to 15 cm wide and a few additional narrow breccia zones (Fig. 3b).

Shear strain of the fault-bounding blocks

The study area is cut by many quasi-planar, sub-vertical fractures with a general E–W trend (Katz et al., 2003). Fractures of this set were displaced and flexed due to slip along the N–S-trending faults like GF2 (Fig. 2) and GF3 (Fig. 3). We measured the flexed traces of some of these fractures in the field in a two-step procedure. First, we aligned a thin thread to the fracture trace on both its sides (x axis in Fig. 4), and then we measured the deviation of the fracture trace from the linear thread as a function of distance from the fault (v(x) in Fig. 4). The flexed fracture traces are assumed to have been linear and continuous prior to faulting, and thus the measured deviations could be used to calculate the continuous shear strain in the blocks. Three flexed traces of fractures were measured across GF2 (marked with gray arrows in Fig. 2a) using the above technique. Fault GF3 is much larger than GF2, and the associated fracture flexing extends to a larger distance. We measured here one flexed swarm of fractures that extends to distances of tens of meters. This swarm is 10–20 cm wide and the measurement was conducted by using an EDM total station system to map the position of its central line.

The measurements are presented in the coordinate system of Fig. 4, where x and y are fault-normal and fault-parallel axes, respectively, v(x) is the fault-parallel measured deviation from a reference line that is normal to the fault, and 2W is the width of the noticeable deviations for a fault of length L (Fig. 5). Figure 5a is a line drawing of the measured deviations [v(x)] of the three fracture traces across GF2 (thick, solid lines on both sides of the fault). At distances of 0.2–0.4 m away from the fault, the deviations from linearity are negligible, and the line deviation increases non-linearly towards the fault. The deviation [v(x)] of fracture traces across GF2 reaches values of 4–11 mm at the fault, equal to half the local slip (Fig. 2b). The deviation [v(x)] of the displaced fracture swarm across GF3 (Fig. 5b) displays similar relations but with larger dimensions. The deviation vanishes at distances of 4–6 m away from the fault, and it gradually increases towards the fault to a maximum deviation of 0.4–0.75 m at the fault. Thus, the width over which the trace is distorted, 2W in Fig. 4, is ~0.5 m for GF2 and up to 10 m for GF3 (Fig. 5).

The flexed traces measured in the field can be fitted by a curve of the form

$$|v(x)| = a \times \exp(b\,|x|) + c \qquad (1a)$$

where a, b, and c are constants; a is approximately the displacement at the fault, and c is a correction factor for the reference line (because the measured fractures or swarm of veins are not necessarily normal to the fault). An example of the curve (eq 1a) is plotted as a dashed curve in Fig. 5a. If we assume that the observed flexure was formed by simple shear, γ, parallel to the fault, then the magnitude of this simple shear can be calculated from the relation

$$\gamma = \delta v/\delta x \qquad (1b)$$

Applying this relation to the flexure curve of eq 1a yields the simple shear magnitude as a function of distance from the fault

$$\gamma(x) = a \times b \times \exp(b\,|x|) \qquad (1c)$$

The calculated simple shear values for the four measured flexed fractures are plotted in Fig. 6.

Probably the most striking feature of the deviated fracture traces of Fig. 5 is their reverse sense of shear with respect to the shear along the fault. The shear that is needed to flex the E–W fracture traces from an initial reference line [$v_0(x) = 0$ for all x] into the current shape is a left-handed shear (gray arrows in Fig. 4). This sense of shear is opposite to the right-lateral shear along the associated fault GF2 or GF3. Following our definition in the Introduction (Fig. 1c), the flexed traces from Gevanim dome are field examples of reverse drag.

3. TIMING, HOST-ROCK RHEOLOGY, AND MECHANISM OF REVERSE DRAG

The above field observations of reverse drag raise several questions: What is the time of the reverse

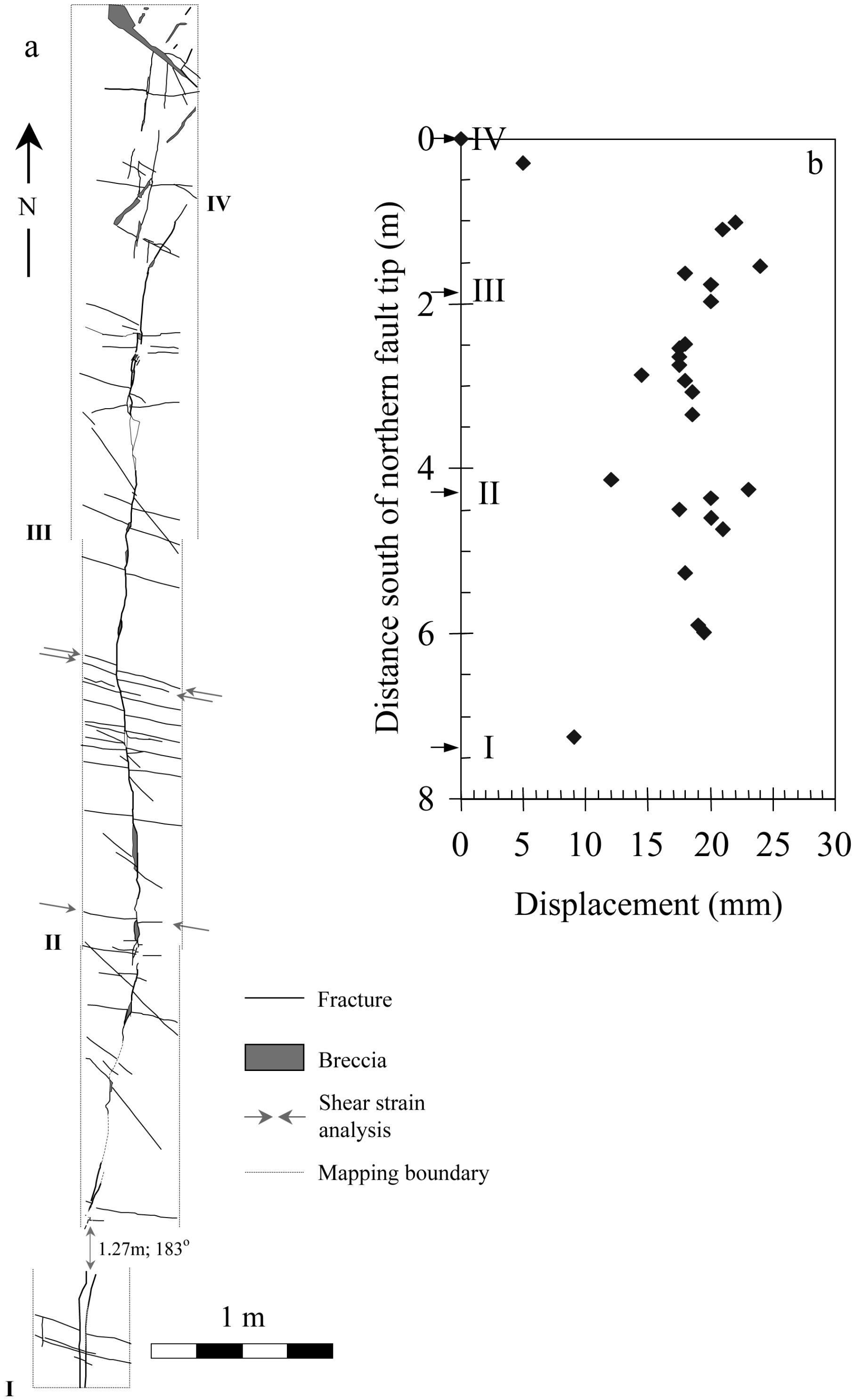

Fig. 2. Gevanim Fault #2 (GF2) (a) Map, 1:10 mapping scale, displaying fault trace and E–W fractures (reproduced from Katz et al., 2003); marked by gray arrows are the E–W fractures used to measure fracture distortion near the faults. (b) Displacement along GF2 from offset E–W fractures, plotted with respect to distance from northern fault tip; Roman numerals indicate locations shown in (a).

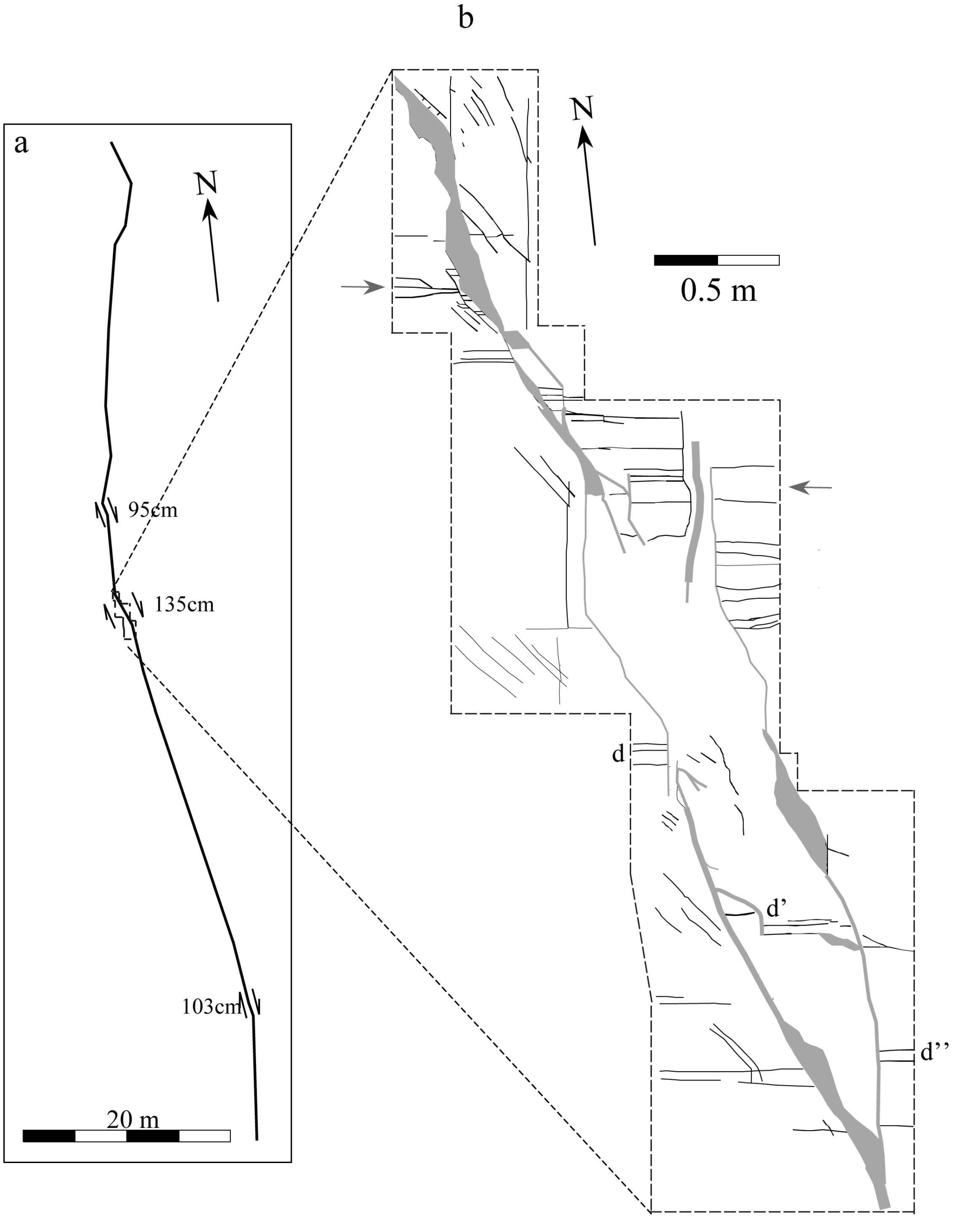

Fig. 3. Gevanim Fault #3 (GF3). (a) Fault trace mapped at 1:500 scale using EDM Total Station. Right lateral displacements are marked. (b) Map, 1:10 mapping scale, displaying fault trace (reproduced from Katz et al., 2003). E–W fractures marked by gray arrows are the ones used to measure fracture distortion near the faults (legend in Fig. 2a). Note offset of groups of E–W fractures, i.e., group d is displaced 0.65 m to group d' on the western segment and again 0.45 m to group d'' on the eastern segment; additional displacement of 0.15 m is distributed between the segments.

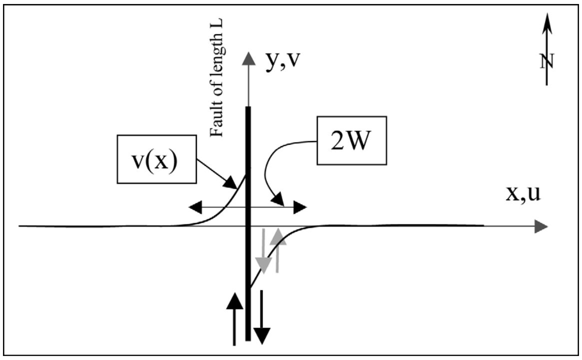

Fig. 4. Idealized presentation of a distorted linear fracture in proximity to GF2. Heavy N–S line—GF2 fault; thin curved line marked v(x)—an E–W-trending fracture distorted near the fault; black arrows—right-lateral slip along GF2; gray arrows- left-lateral shear associated with the distortion of the fracture. The coordinate system of deformation analysis: x, y—fault-normal and fault-parallel axes, respectively; u, v—corresponding displacements; v(x)—fault-parallel displacement; 2W—width of distortion zone.

dragging: prior to faulting, during fault propagation, or during slip along an existing fault? What is the effect of host-rock rheology on this phenomenon (note that Fig. 1 displays ductile plasticene, whereas Fig. 5 diplays brittle rocks at shallow depth). Further, what is the mechanism that allows for contrasting senses of shear to develop next to each other? Some of these questions can be answered by the physical modeling and numerical simulations outlined below.

Reverse drag in laboratory experiments

Odonne (1990) ran a series of experiments with thin plates of wax (70 cm by 45 cm and 1.1 cm thick) subjected to plate-parallel shortening under room conditions. The plates were pre-cut by a 25-cm-long fault that was oriented at 30° to the maximum shortening. A rectangular network of lines parallel to the plate margins was marked on the plate surface prior to loading (Fig. 7a). The shortening of the plate generated shear and normal stresses along the existing fault and these stresses caused slip with maximum value of 65 mm (Fig. 7a). This slip occurred while the slipping fault did not propagate into the solid wax that surrounded both its tips. The rectangular network marked on the plate was distorted uniformly at a distance from the fault and nonuniformly very near the fault (Fig. 7a, b). The distortion of the network lines close to the fault indicates right-lateral shear (white arrows in Fig. 7a) while the fault itself displays left-lateral slip (black arrows in Fig. 7a). In other words, the network displays reverse drag similar to that of Figs. 1 and 5.

While these results of Odonne are apparently the clearest experimental observations of reverse drag, a similar deformation style was observed in other experiments. Freund (1974) tested the deformation of a faulted block of plasticene that was subjected to pure-shear boundary conditions with maximum shortening as high as –0.5 (Fig. 1). During deformation the faults slipped, rotated, and deformed into a sigmoidal shape (Fig. 1b) but did not propagate into the plasticene matrix. Reches and Eidelman (1995) analyzed the deformation of the network marked on Freund's samples. They noted the occurrence of local reverse drag in at least five sites in the experiment, with faults initially oriented at 30º to the maximum shortening (Fig. 1b). Doblas (1990) examined the strain at the proximity of faults that were precut into samples of wax and also noted the development of reverse drag.

These cited experiments have some central properties in common. First, all the faults were cut into the samples prior to the applied deformation. Second, these faults did not propagate into the matrix around them. Third, the samples were made of ductile materials that can accommodate large amounts of strain; for example, the longitudinal maximum strain was –0.44 in Odonne (1990) and –0.5 in Freund (1974). The first two points clearly indicate that the reverse drag forms along existing faults and it does not belong to either the pre-faulting stage or to the propagation stage. The last point is related to the effect of the rheology: Is reverse drag restricted to large deformation of ductile materials? The rheology effect is examined in the next section.

Reverse drag in numerical models

Reches and Eidelman (1995) analyzed the deformation along existing faults with finite element calculations. Their models are for rectangular elastic-plastic plates that include planar faults with friction $\mu = 0.0, 0.5, 1.0$. The results for these calculations are plotted in Fig. 8 as normalized fault parallel displacement versus normalized distance. The calculated flexed lines of Fig. 8 are almost identical in sense and relative magnitude to the above presented field observations of Gevanim dome (Fig. 5) and the experimental results of Odonne (Fig. 7). Reches and Eidelman also showed that the intensity of the reverse drag in the proximity of the "weak" fault ($\mu = 0.0$) is larger than the reverse drag along a "strong" fault ($\mu = 1.0$) (Fig. 8).

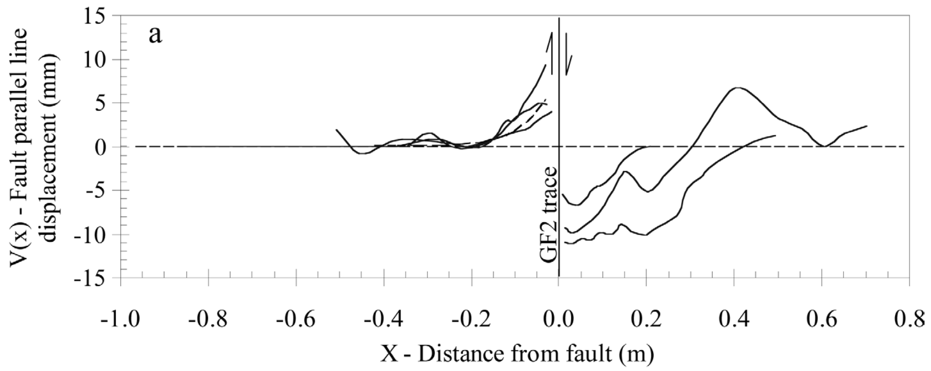

Fig. 5. Line distortion across GF2 and GF3; coordinates defined in Fig. 4, dashed horizontal line in the x coordinate is a reference line. (a) Three field measured profiles of fracture traces across GF2 (locations in Fig. 2); shown is fault-parallel line displacement, v(x), with respect to initial position; thin dashed line on left side of the plot is an exponential regression curve (eq 1a, where a is 9.04, b is –0.02, and c is zero) calculated for one distorted trace (uppermost) on the western side of the fault. (b) A distortion profile measured across GF3; diamonds are points measured on a fracture swarm with EDM Total Station (locations in Fig. 3). Displacement exaggeration of v(x) is the same in (a) and (b); negative/positive x values indicate distance west/east of the fault and negative/positive V(x) values indicate southward/northward fault-parallel displacement.

Grasemann and Stuewe (2001) used the finite-element method to simulate line deformation in the proximity of planar structures such as fault-zones, shear bands, and dikes embedded in a viscous matrix. The calculations were for fault-zones that are 100 times less viscous (weak fault) or 100 times more viscous (strong fault) than the viscous matrix. The numerical results clearly indicate that "reverse drag" develop only along the "weak fault" models (fig. 5a in Grasemann and Stuewe, 2001).

Another type of rheology was used by our dislocation calculations of the fault-normal displacements across a fault in a linear-elastic medium. The model includes a vertical dislocation within an elastic half-

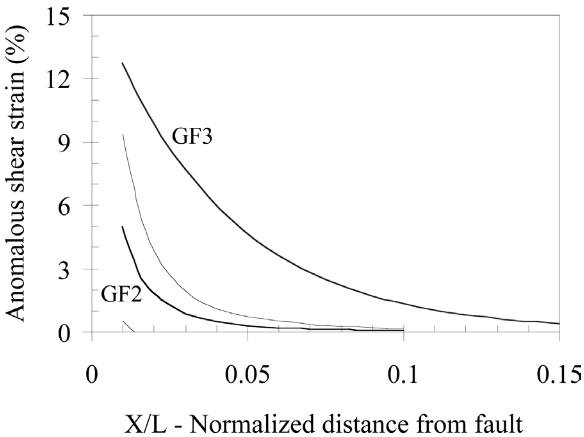

Fig. 6. Reverse drag strain calculated from distorted line at the proximity of GF2 and GF3. The GF2 results (lower curves) are the average of the three analyzed fracture traces (heavy line) with one standard deviation (two thin lines); coordinates are defined in Fig. 4.

space (Erickson, 1987). We checked dislocations ranging in length from 0.25 m to 10 m, in depth from 0.05 m to 100 m, and with 20 mm displacement (as observed across GF2). The calculated fault-parallel displacements of a fault-normal line at the center of the dislocation are presented in Fig. 7b for 0.5 m long and 0.5 m deep dislocation. The slip along the dislocation again displays reverse drag in its proximity.

The above calculations were for faults cut into various types of matrix rheology: elastic-plastic, viscous, or linear-elastic (Fig. 7b). Yet, all revealed that the fault-bounding blocks deformed exclusively by reverse drag regardless of the matrix or fault rheology. We thus conclude that the rheology of the matrix does not control the development of reverse drag.

4. DISCUSSION

The common features in all the above cases of reverse drag are: (1) a weak fault; (2) fault of finite length; (3) the fault exists prior to loading; and (4) the fault does not propagate during the loading. We think that these features are the source of the reverse drag regardless of the matrix rheology. Consider the idealized model of a finite length fault (Fig. 9a) subjected to fault-parallel shear. At first the region is deformed uniformly, reflecting the applied uniform strain (Fig. b). Slip occurs along the fault when its shear strength is exceeded. When this slip occurs, the fault-bounding blocks also deform (Fig. 9c). Paradoxically, the sense of shear in these blocks *must* be opposite to the sense of applied shear and sense of fault slip. This requirement reflects the fact that a fault of finite length affects only a small portion of the entire deformed region. For example, the fault-normal lines in Figs. 5, 7, and 8 do not change their shape or position away from the fault. In qualitative terms, the fault-bounding blocks must shear in the opposite direction to "compensate" for the localized slip along the fault. This "compensation" is a *kinematic requirement* that does not depend on the bulk rheology of the host rock. Thus, one can find striking similarities between the faults in viscous, elastic-plastic, elastic, and more complex materials (Fig. 7b). We also note that the *intensity* of the reverse drag depends on the host rock rheology. For example, friction coefficient affects the intensity of the reverse drag (Fig. 8), and viscous and plastic materials develop large, permanent reverse drag (e.g., Figs. 1 and 7a).

The forgoing discussion of the reverse drag leads to three deductions. First, as the reverse drag is opposite to the sense of fault slip, this shear cannot be related to the *pre-faulting* damage. Second, a striking similarity exists between the reverse drag observed in Gevanim faults and the reverse drag documented along faults embedded in viscous and plastic plates (Fig. 7 and corresponding text). We thus deduce that the rocks in the damage zone of Gevanim faults (Katz et al., 2003) underwent a significant amount of strain *during* slip and *after* the faults were established. It is likely that the accommodation of this large strain was facilitated by the reduction of the rock competence by 30–50% in the damage-zone, as demonstrated in Katz et al. (2003). Third, the numerical simulations of Reches and Eidelman (1995) and Grasemann and Stuewe (2001) indicate that reverse drag is restricted to slip along faults that are significantly weaker than the host rocks.

Finally, we can identify the evolution of the fault-related deformation in Gevanim dome in the Ramon area. Katz et al. (2003) found no evidence for extensive pre-faulting deformation, and proposed that the pre-faulting deformation is limited to shear microfractures observed in the damage zone, which ranges to a fault-normal distance of 0.05–0.06 of the fault length (L). Then, during the faulting stage, the propagating faults generated highly localized deformation in the process zone, 0.001 L wide, manifested primarily as micro-breccia and high shear in the fault-core. Finally, the post-faulting slip along the existing, weak faults generated the reverse drag, as determined for faults GF1 and GF3 (Fig. 5).

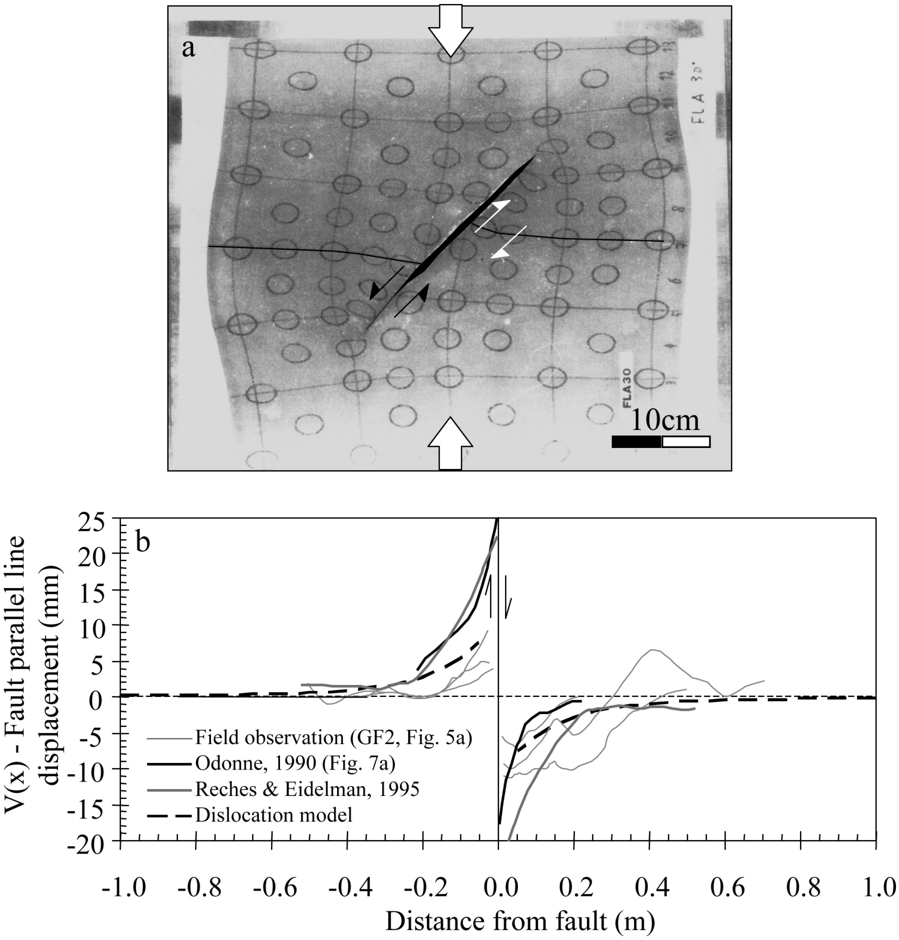

Fig. 7. Experimental, field, and numerical occurrences of reverse drag. (a) A wax plate with a pre-cut fault loaded sub-parallel to its surface (Odonne, 1990); black arrows indicate sense of fault slip; white arrows indicate shear sense within the fault-bounding blocks. (b) Fault-parallel line displacement across GF2 with respect to initial position (thin gray lines, also shown in Fig. 5a); coordinates are defined in Fig. 4. Also included are distorted lines in wax experiments (Odonne, 1990) (solid black lines and a), numeric simulation for an elastic-plastic plate (Reches and Eidelman, 1995) (solid gray line) (friction = 0.0; see text and Fig. 8), and calculation for dislocation model in elastic medium (dashed black line) (see text). All data points are plotted at actual dimensions.

ACKNOWLEDGMENTS

This paper is dedicated to the memory of Dr. Nachman Schulman, the Structureal Geology teacher and M.Sc. advisor of the second author (Z.R.). Nachman combined encyclopedic knowledge and a didactic approach that made him a critical listener and an outstanding teacher. Thanks, Nachman.

This study was partially supported by United States-Israel Binational Science Foundation grant 1998-135, and by the Geological Survey of Israel. We thank Gerhard Oertel and Amotz Agnon for constructive reviews that significantly improved the quality of this manuscript.

REFERENCES

Aydin, A., Johnson, A.M. 1978. Development of faults as zones of deformation bands and as slip surfaces in sandstone. Pure and Applied Geophysics 116: 931–942.

Caine, J.S., Evans, J.P., Forster, C.B. 1996. Fault zone architecture and permeability structure. Geology 24: 1025–1028.

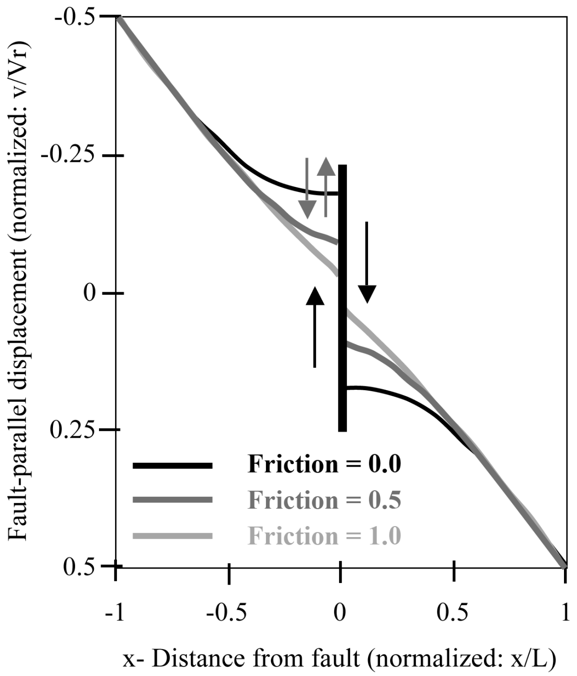

Fig. 8. Finite-element calculations for fault-parallel displacement, v, along a line originally normal to a fault of length (Reches and Eidelman, 1995). Vertical solid black line is the fault of length L. Black thin arrows indicate sense of fault slip and gray thin arrows indicate shear sense in the fault-bounding-blocks. The 0.0, 0.5, and 1.0 values are friction coefficients of the fault. Distance from the fault is normalized by the fault length, x/L, and the fault parallel displacement is normalized by the remote displacement, v/Vr where Vr is the remote displacement (after Reches and Eidelman, 1995).

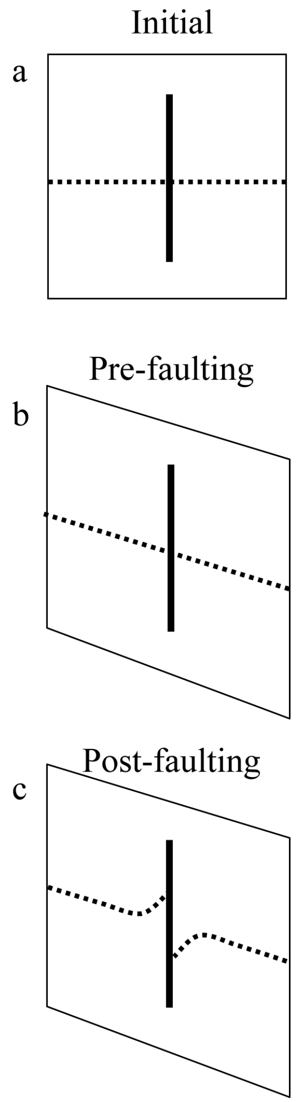

Fig. 9. Schematic presentation of the origin of reverse drag in a plate with a weak fault of finite length (solid vertical line) as manifested by the distortion of a fault-normal line (dashed line) during fault slip. (a) Initial shape. (b) Uniform deformation. (c) The fault slips and the fault-bounding blocks must shear at the fault proximity to compensate for the finite size of the fault (see text). The sense of shear in the blocks is opposite to the sense of applied shear and fault slip, in agreement with Figs. 5, 7, 8.

Chester, F.M., Logan, J.M. 1986. Implications for mechanical properties of brittle faults from observations of the Punchbowl fault zone, California. Pure and Applied Geophysics 124: 79–106.

Davis, G.H., Ryenolds, S. 1996. Structural geology of rocks and regions, 2nd ed. 776 pp.

Doblas, M. 1990. Efecto de arrestre aparente en zonas de cizalla: resultados de un modelo experimental. Geogaceta 8: 30–32 (in Spanish, English abstr.)

Erickson, L. 1987. A three-dimensional dislocation program with application to faulting in the Earth. Applied Earth Science Department, Stanford University, California.

Freund, R. 1974. Kinematics of transform and transcurrent faults. Tectonophysics 21: 93–134.

Grasemann, B., Stuewe, K. 2000. The development of flanking folds during simple shear and their use as kinematic indicators. Journal of Structural Geology 23: 715–724.

Hamblin, W.K. 1965. Origin of 'reverse drag' on the down–throwing side of normal faults. Geological Society of America Bulletin 76: 1145–1164.

Katz, O. 2002. Mechanisms of fault nucleation in brittle rocks. Ph.D. dissertation, Hebrew Univ., Jerusalem. 88 pp.

Katz, O., Reches, Z., Baer, G. 2003. Faults and their associated host rock deformation: Part I. Structure of small faults in a quartz–syenite body, southern Israel. Journal of Structural Geology 25: 1675–1689.

Lyakhovsky, V., Ben–Zion, Y., Agnon, A. 1997. Distributed damage, faulting and friction. Journal of Geophysical Research 102: 27635–27649.

Odonne, F. 1990. The control of deformation intensity around a fault; natural and experimental examples. Journal of Structural Geology 12: 911–921.

Passchier, C.W. 2001. Flanking structures. Journal of Structural Geology 23: 951–962.

Reches, Z., Eidelman, A. 1995. Drag along faults. Tectonophysics 247: 145–156.

Suppe, J. 1985. Principles of structural geology. Prentice–Hall, Upper Saddle River, NJ, 537 pp.

Vermilye, J.M., Scholz, C.H. 1998. The process zone; a microstructural view of fault growth. Journal of Geophysical Research 103: 12,223–12,237.